Double photoionization of a hydrogen molecule at unequal energy sharing

A. S. Kheifets

Research School of Physical Sciences,

*The Australian National University, Canberra ACT 0200, Australia**

Igor Bray

Centre for Atomic, Molecular, and Surface Physics,

School of Mathematical and Physical Sciences,

Murdoch University, Perth, 6150 Australia †

(Dated: March 14, 2005)

Abstract

A recently developed single-center model of double photoionization (DPI) of the H_2 molecule [Phys. Rev. A **71**, 022704 (2005)] has been extended to represent the DPI process at unequal energy sharing. The model is applied to describe the shape of the fully-differential cross-section of a randomly oriented hydrogen molecule in the isotopic form of D_2 at the kinematics of recent experiments.

*Electronic address: A.Kheifets@anu.edu.au; URL: http://rsphysse.anu.edu.au/~ask107

†Electronic address: I.Bray@murdoch.edu.au; URL: http://atom.murdoch.edu.au

I. INTRODUCTION

Significant progress has been achieved very recently in the theoretical description of double photoionization (DPI) of the H_2 molecule. Various *ab initio* non-perturbative methods have been applied to describe this process such as time-dependent close-coupling (TDCC) [1], convergent close-coupling (CCC) [2] and exterior complex scaling (ECS) with B-splines [3]. The TDCC and ECS methods were used to evaluate the integrated DPI cross-section in a fairly good agreement with experiment [4, 5] but far below the earlier calculations of Le Rouzo [6, 7]. The fully differential cross-sections which are much more computationally demanding are yet to be evaluated by these methods. Within the ECS formalism, this will require much larger angular momenta to be taken into account [3].

The CCC model for H_2 combines a multiconfiguration expansion of the molecular ground state with the CCC description of the two-electron continuum which is only correct in the asymptotic region of large distances. Such a model may not correctly predict the magnitude of the DPI cross-sections owing to substantial gauge dependence as was the case with the BBK asymptotic theory [8]. The strength of the CCC model is in its ability to account for the angular correlation in the two-electron continuum and to reproduce correctly the shape of the fully-differential cross-sections (FDCS). This was demonstrated in the kinematics of recent DPI experiments on the randomly oriented and fixed in space hydrogen molecule in the isotopic form of D_2 [9–11]. So far, the CCC theory was tested under the equal energy sharing condition. This is a somewhat special case since the antisymmetric ionization amplitude vanishes at these kinematics. The DPI data for H_2 have been reported for unequal energy sharing as well where 25 eV excess energy was shared between a slow "reference" electron detected in coincidence with a fast variable angle electron [12, 13]. The data complementary to this kinematics were reported by Weber [14] who measured angular distributions of the slow electron in coincidence with a fast reference electron. In this paper, we expand the CCC model to deal with such kinematics and present results of our calculations in comparison with the experimental data of Seccombe et al. [13] and Weber [14]. To test the accuracy and convergence of the CCC method, we utilized two different sets of basis functions. One basis was built from the Laguerre functions as described by

Kheifets [2]. The second calculation was performed using a recently implemented box-state basis [15]. Excellent agreement between the two sets of calculations would assure the quality of the CCC final state.

II. FORMALISM

The single-center CCC model of H_2 DPI was described in detail by Kheifets [2]. In brief, we use a multiconfiguration expansion of the molecular ground state

$$\Psi_0(\boldsymbol{r}_1,\boldsymbol{r}_2)=\sum_{J_0=0,2}\sum_{nl,n'l'}N_{nl,n'l'}\;C_{nl,n'l'}\;\sum_{mm'}C^{J_0M_0}_{lm,\,l'm'}\phi_{nlm}(\boldsymbol{r}_1)\;\phi_{n'l'm'}(\boldsymbol{r}_2) \tag{1}$$

built on the symmetrized pairs of the normalized Slater orbitals:

$$\phi_{nlm}(\boldsymbol{r},\zeta)=(2\zeta)^{n+1/2}\;[(2n)!]^{-1/2}\,r^{n-1}\,e^{-\zeta r}\,Y_{lm}(\boldsymbol{r}) \tag{2}$$

In Eq. (1), the normalization factor $N_{nl,n'l'}=2^{-1/2}\;(1+P_{12})$ for $nl\neq n'l'$ and $N_{nl,n'l'}=1$ otherwise, P_{12} denotes the spatial exchange operator, $C_{nl,n'l'}$ are configuration mixing coefficients given by Hayes [16] for equilibrium interatomic distance of $R=1.4$ a.u.

We build the CCC final state from the two-electron channel states each of which is composed of a target bound state f and a continuum state $\boldsymbol{k}$:

$$\Psi_f(\boldsymbol{k})=|\boldsymbol{k}f\rangle+\sum_j\!\!\!\!\!\!\int d^3k'\frac{\langle\boldsymbol{k}f|T|j\boldsymbol{k}'\rangle|\boldsymbol{k}'j\rangle}{E-k'^2/2-\epsilon_j+i0}. \tag{3}$$

Here $\langle\boldsymbol{k}f|T|j\boldsymbol{k}'\rangle$ is a half-on-shell T-matrix which is found by solving a set of coupled Lippmann-Schwinger equations [17]. We write a dipole matrix element between the ground state and the two-electron continuum state as

$$\langle\Psi(\boldsymbol{k}_1,\boldsymbol{k}_2)|\;d(M_P)\;|\Psi_0\rangle=\sum_{JM}\sum_{l_1l_2}\mathcal{Y}^{l_1l_2}_{JM}(\hat{k}_1,\hat{k}_2)D_{l_1l_2}(E_1E_2)\;(-1)^{M_P}\delta_{M_P+M,\,0} \tag{4}$$

where the bipolar harmonics $\mathcal{Y}^{l_1l_2}_{JM}(\hat{k}_1,\hat{k}_2)=\sum_{m_1m_2}C^{JM}_{l_1m_2,l_2m_2}Y_{l_1m_1}(\hat{k}_1)Y_{l_2m_2}(\hat{k}_2)$, and M_P is the angular momentum projection of the photon. The reduced matrix element is defined by the following projection:

$$D_{l_1l_2}(E_1,E_2)=\langle\Psi_{l_l\,n_2l_2}(k_1)\|D(M_P)\|\Psi_0\rangle\;\langle l_2k_2\parallel l_2n_2\rangle\;, \tag{5}$$

where $\langle l_2 k_2 \parallel l_2 n_2 \rangle$ is the radial overlap between the pseudostate of energy $\epsilon_{n_2 l_2} = E_2$ and the true continuum radial wave function of same energy and angular momentum. We note that in our terminology E_2 is always the energy of the slow or "inner" electron moving in the field of the $Z = 2$ nucleus. The complete set of pseudostates is generated by diagonalizing the target Hamiltonian either on the Laguerre or box-state basis [18].

The matrix elements for the parallel and perpendicular polarization of light in the molecular frame can be written as:

$$\begin{aligned} \langle \Psi(\boldsymbol{k}_1, \boldsymbol{k}_2)| \; z_1 + z_2 \; |\Psi_0\rangle \; &= \; (k_{1z} + k_{2z}) \; g_\Sigma^+ + (k_{1z} - k_{2z}) \; g_\Sigma^- \\ \langle \Psi(\boldsymbol{k}_1, \boldsymbol{k}_2)| \; x_1 + x_2 \; |\Psi_0\rangle \; &= \; (k_{1x} + k_{2x}) \; g_\Pi^+ + (k_{1x} - k_{2x}) \; g_\Pi^- \end{aligned} \tag{6}$$

Expression (6) corresponds to the length gauge of the electromagnetic interaction. Similar expressions can be written for the velocity and acceleration gauges. The symmetric and antisymmetric DPI amplitudes are defined as

$$g^{\pm}_{\Sigma/\Pi} = \frac{\sqrt{3}}{4\pi} \sum_{l=0}^{\infty} \frac{(-1)^l}{\sqrt{l+1}} \left[P'_{l+1}(\cos\theta_{12}) \mp P'_l(\cos\theta_{12}) \right] D^{\pm}_{ll+1}(E_1, E_2), \tag{7}$$

where indices Σ and Π correspond to the parallel ($M_P = 0$) and perpendicular ($M_P = \pm 1$) polarization of light, respectively. Here we introduced symmetric and antisymmetric combinations of the radial matrix elements as

$$D^{\pm}_{l_1 l_2}(E_1, E_2) = \frac{1}{2} \left\{ D_{l_1 l_2}(E_1, E_2) \pm D_{l_1 l_2}(E_2, E_1) \right\}, \tag{8}$$

The M_P dependence is present, but not shown for brevity, in matrix elements (5) and (8). In the laboratory frame, for the light polarized along the z axis, we can write

$$\begin{aligned} \langle \Psi(\boldsymbol{k}_1, \boldsymbol{k}_2)| \; z_1 + z_2 \; |\Psi_0\rangle \; &= \; \cos^2\theta_R \; \left[(k_{1z} + k_{2z}) g_\Sigma^+ + (k_{1z} - k_{2z}) g_\Sigma^- \right] \\ &+ \; \sin^2\theta_R \; \left[(k_{1z} + k_{2z}) g_\Pi^+ + \left[(k_{1z} - k_{2z}) g_\Pi^- \right] \right. \\ &+ \cos\theta_R \sin\theta_R \Big[(k_{1x} + k_{2x}) \; (g_\Sigma^+ - g_\Pi^+) + (k_{1x} - k_{2x}) \; (g_\Sigma^- - g_\Pi^-) \Big] \end{aligned} \tag{9}$$

Here θ_R is the angle of the molecular axis relative to the polarization axis of light taken as the $\boldsymbol{z}$-axis in the laboratory frame. After taking the spherical average over all the molecular orientations, we arrive to Eq. (8) of Seccombe et al. [13]:

$$\begin{aligned} \text{FDCS} \; \propto \; & \frac{2}{15} |\mathcal{C}_\Sigma|^2 + \frac{7}{15} |\mathcal{C}_\Pi|^2 + \frac{6}{15} \text{Re} \; \mathcal{C}_\Sigma^* \mathcal{C}_\Pi \\ & + \frac{1}{15} \Big\{ |g_\alpha|^2 + |g_\beta|^2 + 2 \; \text{Re} \; g_\alpha^* g_\beta \cos(\theta_1 - \theta_2) \Big\}, \end{aligned} \tag{10}$$

where we introduce auxiliary variables for brevity of notations:

$$\begin{aligned} \mathcal{C}_\Sigma &= (k_{1z}+k_{2z})g_\Sigma^+ + (k_{1z}-k_{2z})g_\Sigma^- \\ \mathcal{C}_\Pi &= (k_{1z}+k_{2z})g_\Pi^+ + (k_{1z}-k_{2z})g_\Pi^- \\ g_\alpha &= g_\Sigma^+ - g_\Pi^+ + g_\Sigma^- - g_\Pi^- \quad , \quad g_\beta = g_\Sigma^+ - g_\Pi^+ - g_\Sigma^- + g_\Pi^- \end{aligned}$$

In the case of He, $g_\Sigma = g_\Pi$ and FDCS $\propto |(k_{1z}+k_{2z})g^+ + (k_{1z}-k_{2z})g^-|^2$ As it was noted in the introduction, the present model exhibits a strong gauge dependence. In the following, we present the velocity gauge results as most reliable.

III. RESULTS

A. DPI amplitudes

The moduli of the amplitudes $g^\pm_{\Sigma,\Pi}$ and their relative phases as functions of the interelectron angle θ_{12} are plotted in Figure 1 together with their counterparts for atomic He. The energy of the slow electron is fixed at $E_1 = 2$ eV. Although not plotted in Figure 1, similar angular dependences are displayed at other energy partitions.

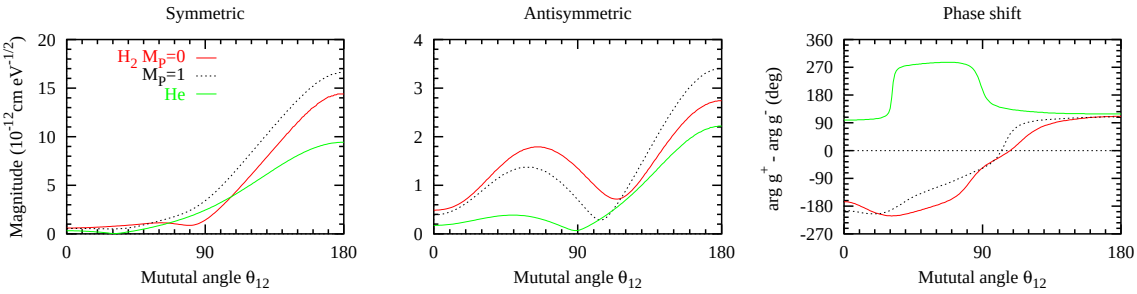

FIG. 1: Moduli of the symmetric (left) and antisymmetric (centre) amplitudes and their relative phases (right) for DPI of He and H_2 at $E_1 = 2$ eV. For H_2, the amplitudes corresponding to parallel ($M_P = 0$) and perpendicular ($M_P = 1$) polarizations of light relative to the molecular axis are shown by red/solid and black/dotted lines. The He amplitudes and their relative phase is shown by green/dashed lines

To make a quantitative characterization of the amplitudes, we notice that the symmetric

amplitudes display a clear Gaussian shape and can be fitted with the Gaussian ansatz

$$\left|g^{+}_{\Sigma,\Pi}\right| = A \ \exp\left[-2\ln 2\frac{(\pi-\theta_{12})^2}{\Delta\theta^2_{12}}\right] \tag{11}$$

Asymmetric amplitudes show considerable "wings" at small mutual angles. We consider these "wings" as artifacts and fit only the central portion of the amplitude at $90 \leq \theta_{12} \leq 180°$ with a Gaussian centered at $\theta_{12} = 180°$. Thus produced, the magnitude A and width $\Delta\theta_{12}$ parameters are shown in Figure 2. The width parameters vary insignificantly with energy partition ratio E_1/E_2. For the symmetric amplitude, $\Delta\theta^{\Pi+}_{12} < \Delta\theta^{\Sigma+}_{12} < \Delta\theta^{\mathrm{He}+}_{12}$ as was previously reported [2]. No similar trend was observed for antisymmetric amplitudes with $\Delta\theta^{\Sigma-}_{12} \simeq \Delta\theta^{\Pi-}_{12} \simeq \Delta\theta^{\mathrm{He}-}_{12}$. As the energy partition E_1/E_2 changes, the symmetric magnitude parameters for parallel (Σ) and perpendicular (Π) orientations vary slightly with a typical ratio $A^{+}_{\Pi}/A^{+}_{\Sigma} \approx 1.2$. Such a small asymmetry is consistent with a relatively small fraction of the $J = 2$ component in the molecular ground state [2]. The antisymmetric magnitude parameters decrease rapidly towards more even energy-sharing with approximately the same asymmetry between the parallel and perpendicular orientations. Relative phase between the symmetric and antisymmetric amplitudes shown in Figure 1 is insensitive to the target at $90 \leq \theta_{12} \leq 180°$, but is quite different for He and H_2 at small interelectron angles in the "wing" region of the antisymmetric amplitudes.

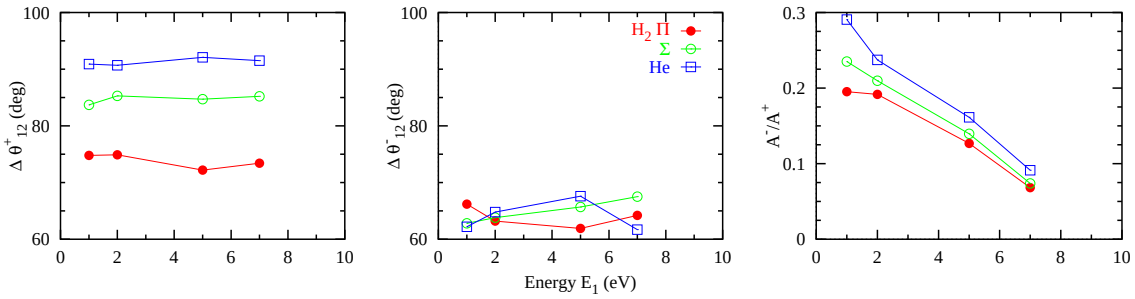

FIG. 2: The left and central panels show the Gaussian width parameters for the symmetric and antisymmetric amplitudes respectively. The right panels show the amplitudes ratio A^{-}/A^{+} in H_2 and He. In molecular hydrogen, parameters of the parallel Σ and perpendicular Π amplitudes are shown separately

B. Fully-differential cross-sections

1. *Slow reference electron*

The fully differential cross-sections in the form of the angular distribution of the fast electron are shown in Figure 3 for He (left - polar and central - Cartesian plots) and H_2 (right panel). Direction of the slow reference electron is chosen along the polarization axis of light $\theta_1 = 0$ and shown by the arrow on the left panels. The He FDCS have a "fish" shape typical for highly asymmetric energy sharings [19]. The evolution of the FDCS with energy partition ratio can be explained by an interplay of the symmetric and antisymmetric amplitudes [20]. The forward lobe corresponding to the back-to-back emission originates solely from the antisymmetric amplitude. With the energy of the slow electron E_1 growing, this amplitude gradually decreases in magnitude and the FDCS becomes dominated by the side lobes originated from the symmetric amplitude. Agreement with experiment for He is generally good but some features of the FDCS cannot be reproduced completely. For instance, the side lobes are too big for $E_1 = 2$ and 5 eV. Similar disagreement can be seen in Fig. 7 of Selles et al. [20]. It is interesting that in their earlier paper [13] the same authors reported a nearly perfect agreement with the experiment, but later retracted their results as not fully converged with respect to the size of the interaction region R_0. As we use two completely different sets of target states, with the box states being extended to R_0 exceeding 100 atomic units, we are confident that our results are fully converged. For $E_1 = 7$ eV, we have the central lobe somewhat below the experiment whereas both calculations [13] and [20] reproduce it very well.

Now we turn to analyzing the H_2 data. As compared to He, the experimental H_2 FDCS have more diffuse shape with a three-lobe structure which is much less prominent. Seccombe et al. [13] suggested that this might be either due to averaging over all molecular orientations or due to the intrinsic differences between the two targets. In our model, the effect of averaging is represented by the terms containing g_α, g_β which are very small due to insignificant anisotropy of the molecular ground state. For $E_1 \leq 5$ eV, the side lobes are still present in the calculated FDCS, but with a lesser intensity in H_2 as compared to He.

For larger $E_1 = 7$ eV, the side lobes dominate the FDCS both for He and H_2.

The difference between the two targets can only be attributed to the Gaussian width of the symmetric amplitude since other amplitude parameters are quite similar in H_2 and He. Angular position of the side lobes is a result of an interplay between the kinematic term $\cos\theta_1 + \cos\theta_2$ which peaks at $\theta_1 = 0$ and the Gaussian term $\exp[-2\ln 2(\pi - \theta_{12})^2/\Delta\theta_{12}^2]$ which peaks at $\theta_1 = \pi$. The product of the kinematic and the Gaussian terms peaks somewhere between these two extremes at an angle depending on the Gaussian width. If the width parameter decreases, this peak moves closer to the central lobe and decreases in magnitude which can be visually interpreted as "diffusion" of the three-lobe structure. At more even energy sharings, when the central lobe is suppressed, the difference of the FDCS in He and H_2 is not so dramatic.

This effect is exemplified in Figure 4 where we plot the ratios of the FDCS in H_2 and He shown previously in Figure 3. Both the calculation and the experimental data of Seccombe et al. [13] are normalized in such a way that the ratio is set to unity at $\theta_1 = 180°$. Here we see a clear peak which indicates the angular position of the side lobes in H_2. Qualitatively, the calculation resembles the experiment except for $E_1 = 7$ eV, where the calculated ratio is much more uniform as compared to the experiment. This, however, might be a result of normalization of the experimental data to a stray point which does not represent the whole set adequately.

2. Fast reference electron

In a recent paper [20], the same experimental group of Reddish and co-workers presented the He FDCS at a complementary geometry where the fast electron is fixed and the angular distribution of the slow electron is detected. These data served as a test bench for the hyperspherical R-matrix calculations of Selles et al. [20]. Unfortunately, no H_2 FDCS were reported at these kinematics. However, here we are are aided by Weber [14] who reported the FDCS for the slow variable angle electron at $E_1 + E_2 = 24.5$ eV. To improve statistics of the experiment, the slow electrons with 10% or less of the total excess energy were binned together. Unlike in the experiments of Reddish and co-workers, several fixed angular

positions of the fast reference electron were recorded with $\theta_1 = 0$, 30°, 60° and 90°.

The He FDCS for complementary geometry and various energy sharings are shown in Figure 5 as polar (left) and Cartesian (right) plots. These FDCS are constructed from the same symmetric and antisymmetric amplitudes as the FDCS shown in Figure 3. However, due to the swap of the reference and variable angle electrons, the interference of the terms containing the symmetric and antisymmetric amplitudes is now constructive with both terms contributing to the same peak with very little internal structure. Physically, this reflects the fact that the slow electron is ejected mainly via the shake-off mechanism and demonstrates little anisotropy. This is in contrast to the fast electron which is ejected due to the absorption of the photon and shows a strong anisotropy relative to the polarization axis of light. These effects are much more pronounced at a higher photon energy [21]. As the energy partition becomes more even ($E_2 = 7$ eV), almost all the contribution to the FDCS comes from the symmetric amplitude and the angular distribution of the fast and slow variable electrons become very similar except for the back-to-back emission.

The H_2 FDCS for $E_1 = 23$ eV and $E_2 = 2$ eV are shown in Figure 6 along with experimental FDCS of Weber [14] for several fixed fast electron angles. Comparison with the experiment is not straightforward since the data for $E_2 \leq 2.5$ eV were binned together. Nevertheless, we believe that a fixed $E_2 = 2$ eV calculation represents the data reasonably well. The evolution of the FDCS with varying angle θ_2 is again explained by the competition of the terms containing the symmetric and antisymmetric amplitudes. At 90° fixed angle, the symmetric amplitude clearly dominates and the FDCS contains two symmetric lobes. Back-to-back emission is forbidden in the He case but can happen in H_2 due to a difference between the Π and Σ amplitudes. This difference, however, is too small in our model to account for a large experimental back-to-back emission in this kinematics. At other fixed angles, agreement with the experiment is satisfactory. We note that the experiment is internormalized and only one scaling constant was used in all plots of Figure 6.

IV. CONCLUSION

In the present work, we tested a CCC-based model developed to describe the DPI FDCS of H_2 in the kinematics of recent experiments at unequal energy sharing. The model employs a single-center expansion of the molecular ground state and a helium-like description of the doubly ionized final state. Satisfactory agreement with the experiment, in terms of the shape of FDCS, indicates that the angular correlation in the two-electron continuum is established at large distances where the separation of the two nuclei can be neglected and they can be viewed as a united helium atom.

In the meantime, the anisotropy of the molecular DPI, which comes in the present model from the single-center ground state, seems to be underestimated. The calculated Π and Σ amplitudes differ by only 20% which is insufficient to account for a strong back-to-back emission in the experiment of Weber [14] and to explain a highly irregular H_2/He FDCS ratio in the experiment of Seccombe et al. [13]. A proper two-center description of the two-electron continuum is needed for better account of such purely molecular effects.

V. ACKNOWLEDGEMENTS

We are grateful to Tim Reddish and Thorsten Weber for communicating their data in numerical form. The authors acknowledge support of the Australian Research Council in the form of Discovery grant DP0451211. Facilities of the Australian Partnership for Advanced Computing (APAC) were used. We are also grateful to ISA Technologies, Perth, Western Australia, for provision of access to their IBM P690 computer in support of this project.

[1] J. Colgan, M. S. Pindzola, and F. Robicheaux, J. Phys. B **37**, L377 (2004).

[2] A. S. Kheifets, Phys. Rev. A **71**, 022704 (2005).

[3] W. Vanroose, F. Martin, T. N. Rescigno, and C. W. McCurdy, Phys. Rev. A **70**, 050703 (2004).

[4] G. Dujardin, M. J. Besnard, L. Hellner, and Y. Malinovitch, Phys. Rev. A **35**, 5012 (1987).

[5] H. Kossmann, O. Schwarzkopf, B. Kämmerling, and V. Schmidt, Phys. Rev. Lett. **63**, 2040 (1989).

[6] H. Le Rouzo, J. Phys. B **19**, L677 (1986).

[7] H. Le Rouzo, Phys. Rev. A **37**, 1512 (1988).

[8] S. P. Lucey, J. Rasch, C. T. Whelan, and H. R. J. Walters, J. Phys. B **31**, 1237 (1998).

[9] J. P. Wightman, S. Cvejanović, and T. J. Reddish, J. Phys. B **31**, 1753 (1998).

[10] T. Weber, A. Czasch, O. Jagutzki, A. Müller, V. Mergel, A. Kheifets, J. Feagin, E. Rothenberg, G. Meigs, M. Prior, et al., Phys. Rev. Lett. **92**, 163001 (2004).

[11] T. Weber, A. Czasch, O. Jagutzki, A. Müller, V. Mergel, A. Kheifets, E. Rothenberg, G. Meigs, M. Prior, S. Daveau, et al., Nature **431**, 437 (2004).

[12] S. A. Collins, A. Huetz, T. J. Reddish, D. P. Seccombe, and K. Soejima, Phys. Rev. A **64**, 062706 (2001).

[13] D. P. Seccombe, S. A. Collins, T. J. Reddish, P. Selles, L. Malegat, A. K. Kazansky, and A. Huetz, J. Phys. B **35**, 3767 (2002).

[14] T. Weber, Ph.D. thesis, Universität Frankfurt, Institut für Kernphysik (2003).

[15] I. Bray, K. Bartschat, and A. T. Stelbovics, Phys. Rev. A **67**, 060704(R) (2003).

[16] E. F. Hayes, J. Chem. Phys. **46**, 4004 (1967).

[17] I. Bray and A. T. Stelbovics, Adv. Atom. Mol. Phys. **35**, 209 (1995).

[18] I. Bray, K. Bartschat, D. V. Fursa, and A. T. Stelbovics, J. Phys. B **36**, 3425 (2003).

[19] O. Schwarzkopf, B. Krassig, V. Schmidt, F. Maulbetsch, and J. S. Briggs, J. Phys. B **27**, 4817 (1994).

[20] P. Selles, L. Malegat, A. Huetz, S. A. Collins, D. P. Seccombe, and T. J. Reddish, Phys. Rev. A **69**, 052707 (2004).

[21] A. Knapp, A. Kheifets, I. Bray, T. Weber, A. L. Landers, S. Schössler, T. Jahnke, J. Nickles,

S. Kammer, O. Jagutzki, et al., Phys. Rev. Lett. **89**, 033004 (2002).

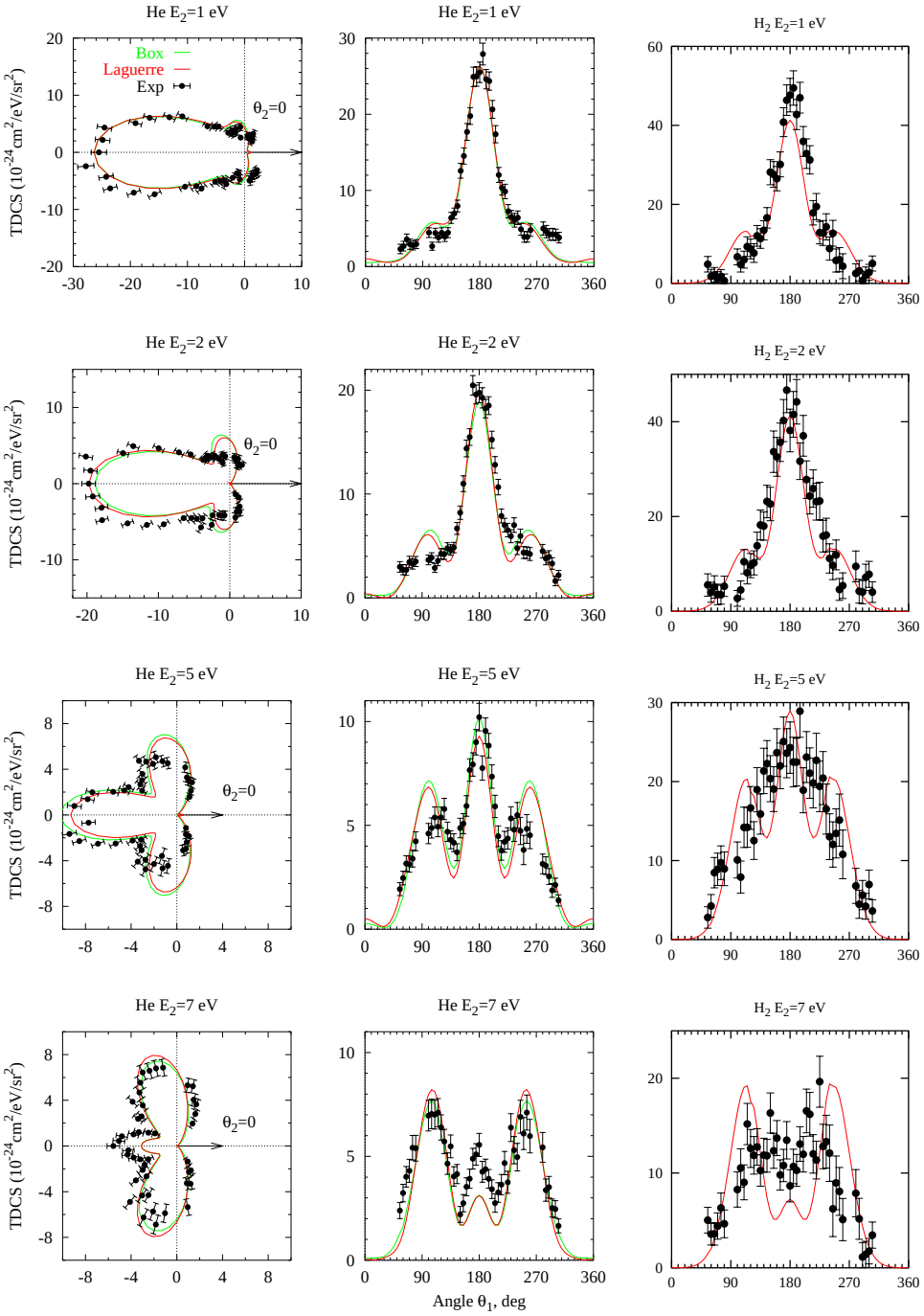

FIG. 3: Angular distribution of the fast electron E_1 is plotted with the slow electron E_2 being fixed along the polarization axis of light (horizontal). The box states (red/solid line) and Laguerre (green/dashed line) calculations are presented along with the experiment of Seccombe et al. [13]. The left and middle panels show helium FDCS in the polar and Cartesian coordinates. The right panel shows the Cartesian plots for H_2.

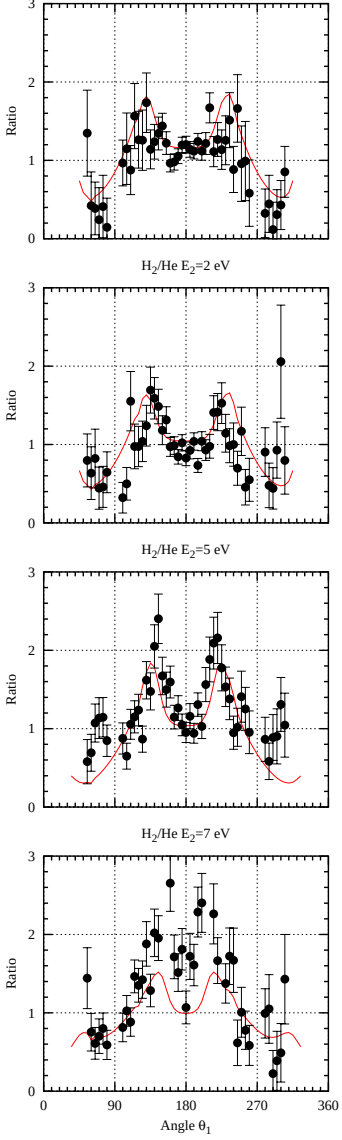

FIG. 4: Ratios of the FDCS in H_2 and He shown in Figure 3. The ratios are normalized to unity at $\theta_2 = 180°$. Experimental data are due to Seccombe et al. [13]

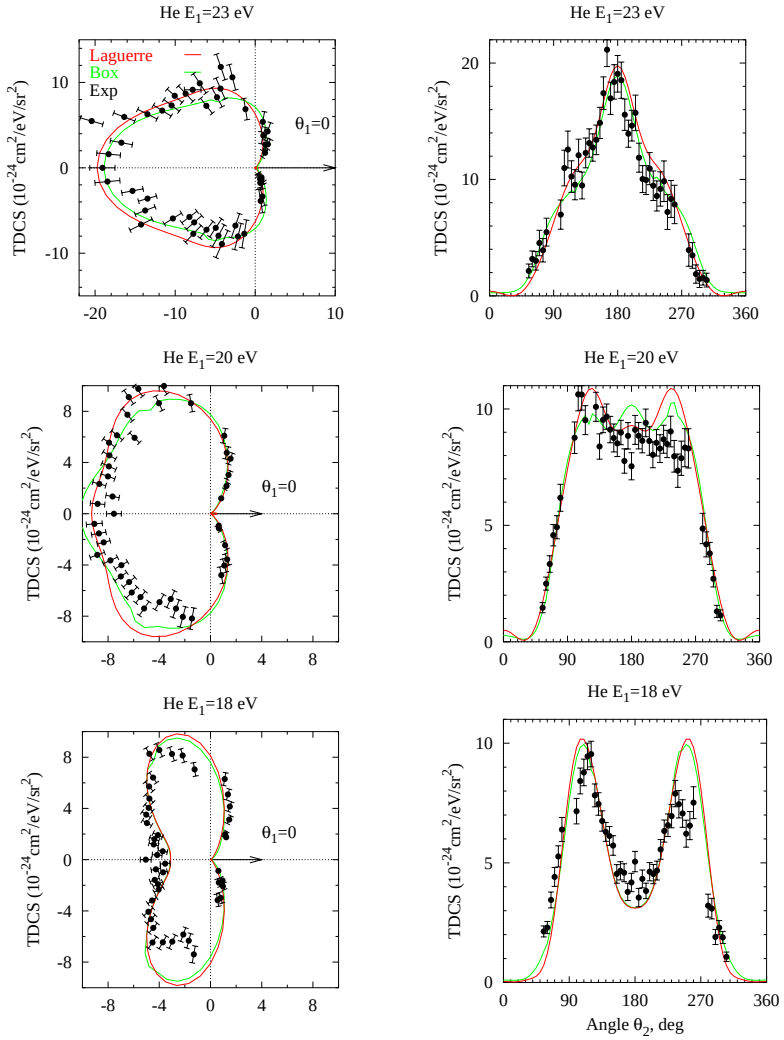

FIG. 5: The He FDCS for the slow variable angle electron and the fast reference electron. Experimental data are from Selles et al. [20]

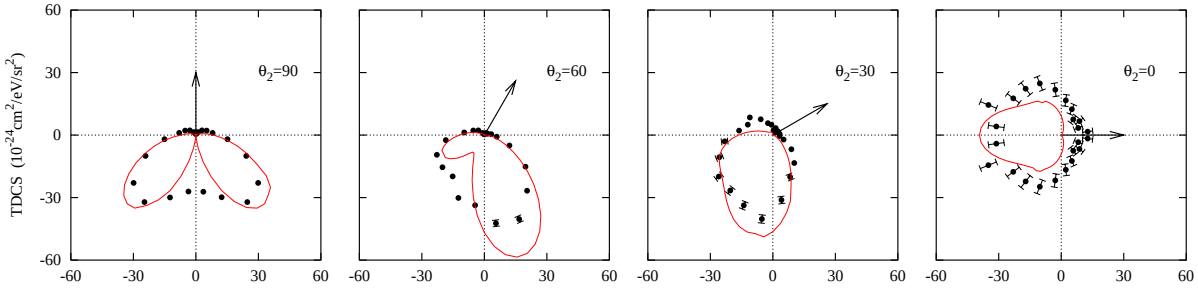

FIG. 6: The H_2 FDCS for the slow $E_2 = 5$ eV variable angle electron and the fast $E_1 = 20$ eV reference electron. Experimental data are from Weber [14]